ELSEVIER

Contents lists available at ScienceDirect

Tribology International

journal homepage: www.elsevier.com/locate/triboint





Structural, mechanical and tribocorrosion behaviors of Mo-Ni-Si alloys

H. Chen*, R.P. Li, L.Y. Liu, Z. Zhang, X.L. Zhao

School of Materials Science and Engineering, Liaocheng University, Liaocheng, Shandong 252000, China

ARTICLE INFO

Keywords: Mo-Ni-Si alloys Tribocorrosion Mechanical properties Intermetallic

ABSTRACT

Mo-Ni-Si alloys were fabricated using arc melting, and their structural and tribocorrosion behaviors were investigated. The results revealed that the alloys have good comprehensive mechanical properties and tribocorrosion resistance with increasing Mo content. The alloys exhibit lower friction coefficients and wear rates owing to the creation of the MoO₃-NiO-SiO₂ passivation layer. The wear rates of the alloys were approximately one-tenth of that of 0Cr18Ni9. During the tribocorrosion tests, the OCP values of the alloys are inversely related to the friction coefficient, which is attributed to the synergistic effect of wear and corrosion. The main tribocorrosion mechanisms for Mo-Ni-Si alloys are pure wear and preferential tribocorrosion of the NiMo phase, whereas the wear loss of 0Cr18Ni9 is dominated by corrosion-induced wear.

1. Introduction

Due to the complexity of aerospace and marine environments, the application of traditional engineering materials is facing increasing challenges [1,2]. Wear and corrosion have become the predominant failure modes of mechanical moving components working in marine environments [3]. Especially when wear and corrosion coexist (as tribocorrosion), their synergistic effects tend to accelerate material failure compared to either effect alone, which leads to increased maintenance costs, high safety risks, and potential environmental pollution [4-6]. However, traditional engineering materials such as cast iron and austenitic stainless steel are hard to apply in tribocorrosion environments due to their inability to achieve both corrosion and wear resistance [7,8]. Some studies have shown that metal silicides and their composites exhibit good wear and corrosion properties due to their high strength, hardness and chemical stability [9-13]. However, as tribocorrosion components, their room temperature fracture toughness needs to be further improved.

In general, the production of multiphase structures and the formation of ternary metal silicides are two feasible methods for improving the toughness of the materials [14]. In the Mo-Ni-Si ternary system, the metal silicide Mo_2Ni_3Si with an hP12 MgZn₂-type crystal structure has a relatively wide range of chemical compositions, high hardness, and better toughness compared to the Mo-Si binary metal silicides [15,16]. Furthermore, the ternary metal silicides Mo_2Ni_3Si are suitable to form "in-situ" composites with the more ductile nickel-based solid solutions $(\gamma-Ni_{ss})$ and molybdenum-based solid solutions (Mo_{ss}) , which can further

improve the room temperature toughness of the metal silicide alloys [17,18]. Wang et al. [19,20] prepared $\gamma\textsc{-Ni}_{ss}/\textsc{Mo}_2\textsc{Ni}_3\textsc{Si}$ "in-situ" composites by laser melting deposition, which significantly improved the room temperature fracture toughness of the composites.

Wear and corrosion resistance should be the first consideration when Mo₂Ni₃Si metal silicides are used as structural materials. From the perspective of mechanical wear, Mo₂Ni₃Si metal silicide was expected to have excellent wear resistance and lubrication properties due to its high hardness, strong atomic bonding and anomalous temperature-strength relationship. [21,22]. In recent years, with the introduction of γ -Ni_{ss}, Moss and NiMo intermetallic compounds, Mo2Ni3Si-based alloys have demonstrated a favorable combination of strength and toughness, endowing the alloys with excellent wear resistance. [23-25]. It is considered that the predominant wear mechanisms for these alloys are preferential wear of interdendritic medium and primary dendrite exfoliation of Mo₂Ni₃Si [26]. In terms of corrosion resistance, metal silicide Mo₂Ni₃Si is anticipated to be a good corrosion-resistant material due to its strong atomic bonds and chemical stability [15]. Moreover, the constituent elements of Mo, Ni, and Si readily form passive layers in acidic and mild solutions, and the passivation layer can effectively impede further erosion in the corrosive solution, which also endows the Mo₂Ni₃Si alloy with excellent corrosion resistance. To the author's knowledge, there is little research literature on the wear and corrosion properties of Mo2Ni3Si alloys, especially on the tribocorrosion properties of Mo2Ni3Si alloys, which have not been reported. In this paper, Mo-Ni-Si alloys were fabricated by vacuum arc melting. The structural

E-mail address: chenhui002@qq.com (H. Chen).

^{*} Corresponding author.

and tribocorrosion performances of Mo-Ni-Si alloys were investigated, and the corresponding tribocorrosion mechanisms were discussed.

2. Experimental procedures

2.1. Materials preparation

Mo-Ni-Si alloy materials were prepared using molybdenum (99.9%), nickel (99.5%), and silicon (99.9%) powders as raw materials (raw powders were supplied by Sinopharm Chemical Reagent Co. Ltd., China). The average particle size of the powders is $30 - 90 \mu m$. The nominal chemical compositions of the alloys are shown in Table 1. The raw powders were mixed in a planetary ball mill. The ball-to-powder ratio was 10:1, the milling rotation speed was 250 rpm, and the milling time was 5 h. The mixed powder was pressed into blocks and then placed in a water-cooled copper crucible and the Mo-Ni-Si alloys were synthesized by arc melting. The detailed melting parameters are as follows: vacuum levels down to 4×10^{-3} Pa, arc current about 500 A, the voltage 11-12 V, and then a 0.5 atm of high-purity gas was filled to act as a protective gas during the melting process. To achieve uniform structure and properties, each ingot was remelted 4-5 times, and the electromagnetic stirring was started when the ingot was melted. Mo-Ni-Si alloy ingots were machined into 10 mm \times 10 mm \times 5 mm samples using an electro-discharge machine (EDM, DK7740-B, Wuhan Xin Dexing CNC Machine Tools Co. Ltd., China), which were sandpaper ground, polished, and ultrasonically cleaned for microstructure observation and tribocorrosion testing.

2.2. Materials characterizations

The microstructures and surface morphology of the Mo-Ni-Si alloys were observed by optical microscope (OM, Axio Scope A1, Germany) and field-emission scanning electron microscope (SEM, JSM-6700 F, JEOL, Japan). The crystal phase structure of the alloys was examined using X-ray diffraction (XRD, D/Dmax-2400, Rigaku, Japan). X-ray diffraction was performed using Cu K α radiation at a wavelength (λ) of 0.15418 nm, and the scanning range and the scanning speed were $20^{\circ} \sim 90^{\circ}$ and 5° /min, respectively. The phase compositions of the alloys were characterized by energy dispersive spectroscopy (EDS). The microhardness of the alloys was determined by a microhardness tester (MHV2000, China) with a load of 9.8 N and a holding time of 10 S. The average of five hardness measurements was taken as the hardness value of the alloys. Meanwhile, the fracture toughness of the Mo-Ni-Si alloys based on the indentation tests was estimated using the formula [27]:

$$K_c = 0.028 \left(\frac{E}{H_y}\right)^{1/2} \cdot \frac{P}{C^{3/2}}$$
 (1)

Where K_c is the fracture toughness of the alloys (MPa·m^{1/2}), E is the modulus of elasticity (MPa), H_v is the material hardness (MPa), P is the load (N), and C is the length of the crack (m).

Nanoindentation tests of Mo-Ni-Si alloys were performed using a G200 nanoindentation instrument (KLA-Tencor Co. Ltd., USA). The maximum applied load for the indentation test was 50 mN and the loading rate was 2.5 mN/s. The type of indentation for the nanoindentation test is a triangular pyramid indentation and the top angle is 115° and the Poisson's ratio is 0.07. For all specimens, nanoindentation

Table 1Chemical composition (at% and wt% were the numbers shown in parentheses) of the experimentally designed alloys.

Samples	Mo	Ni	Si
M-1 (Mo-50Ni-17Si)	33(48)	50(44)	17(7)
M-2 (Mo-46Ni-15Si)	38(54)	46(40)	15(6)
M-3 (Mo-43Ni-14Si)	43(59)	43(36)	14(6)
M-4 (Mo-39Ni-13Si)	49(64)	39(31)	13(5)

tests were conducted in at least 6 different locations to ensure the reproducibility of the data results.

2.3. Tribocorrosion test of the Mo-Ni-Si alloys

Tribocorrosion tests were carried out on Mo-Ni-Si alloys by an electrochemical reciprocating sliding tribometer (MFT-EC4000, Lanzhou Huahui Instrument Technology Co., Ltd., China) at room temperature under open circuit potential (OCP) conditions. The tribocorrosion tests of the alloys were performed in a 3.5 wt% NaCl solution with a three-electrode system, as shown in Fig. 1. The reference electrode, counter electrode, and working electrode were saturated calomel electrodes, high-purity graphite and alloys with an exposure area of 1 cm², respectively. The 6 mm diameter Al₂O₃ ball was chosen as the counterpart, which has the advantages of high hardness, good wear and corrosion resistance, as well as low electrical conductivity in NaCl solution. It can effectively minimize the surface migration of the counterpart material and prevent the occurrence of extra chemical reactions during tribocorrosion tests. Its hardness, elastic modulus and surface roughness (R_a) were 17.2 GPa, 368 GPa and 47.8 nm, respectively. For tribocorrosion tests, the reciprocating frequency was 2 Hz, the reciprocating length was 5 mm, the loads were 2 N, 5 N, and 10 N, and the sliding time was 40 min. The average Hertzian contact pressure of the alloys/ Al_2O_3 balls tribo-pairs was 0.72 - 1.58 GPa. Before the tribocorrosion test, the samples were immersed for at least 1 h to stabilize the OCP values. The OCP values were recorded continuously before and after tribocorrosion for 10 min to evaluate the chemical stability and passivation characteristics of the material surface. Friction coefficients and corresponding OCP variations were automatically recorded by the microcomputer during the tribocorrosion tests. Subsequently, the tribocorrosion depth profile of each track for the alloys was examined by a surface profiler (Alpha Step IQ). To analyze the tribocorrosion mechanisms, pure wear tests were conducted in deionized water under the same conditions as mentioned above. Tribocorrosion tracks and wear debris were observed by SEM and transmission electron microscopy (TEM, TECNAI G2 S-TWIN F20, USA) with an acceleration voltage of 200 kV. For comparative analysis, a reference material (0Cr18Ni9 stainless steel) was selected and its tribocorrosion characteristics were tested under the same conditions. The chemical composition of OCr18Ni9 stainless steel is Fe-18.6%Cr-9.3%Ni-0.1%C (wt%).

3. Results and discussion

3.1. Microstructure characteristics of the Mo-Ni-Si alloys

Fig. 2 depicts the XRD patterns of Mo-Ni-Si alloys. It was seen that

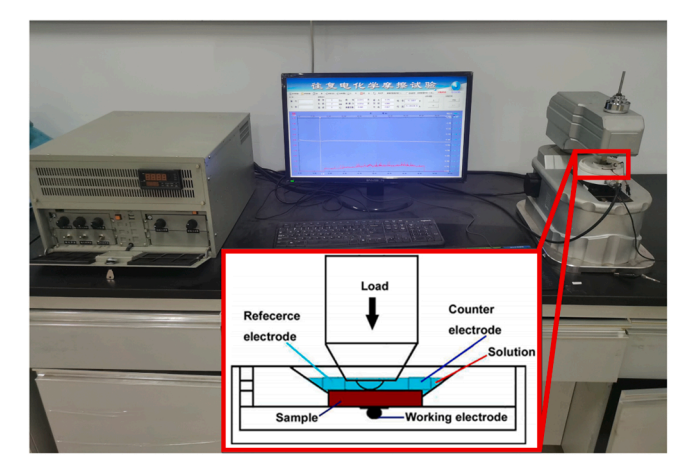


Fig. 1. Schematic diagram of the tribocorrosion apparatus used in this experiment.

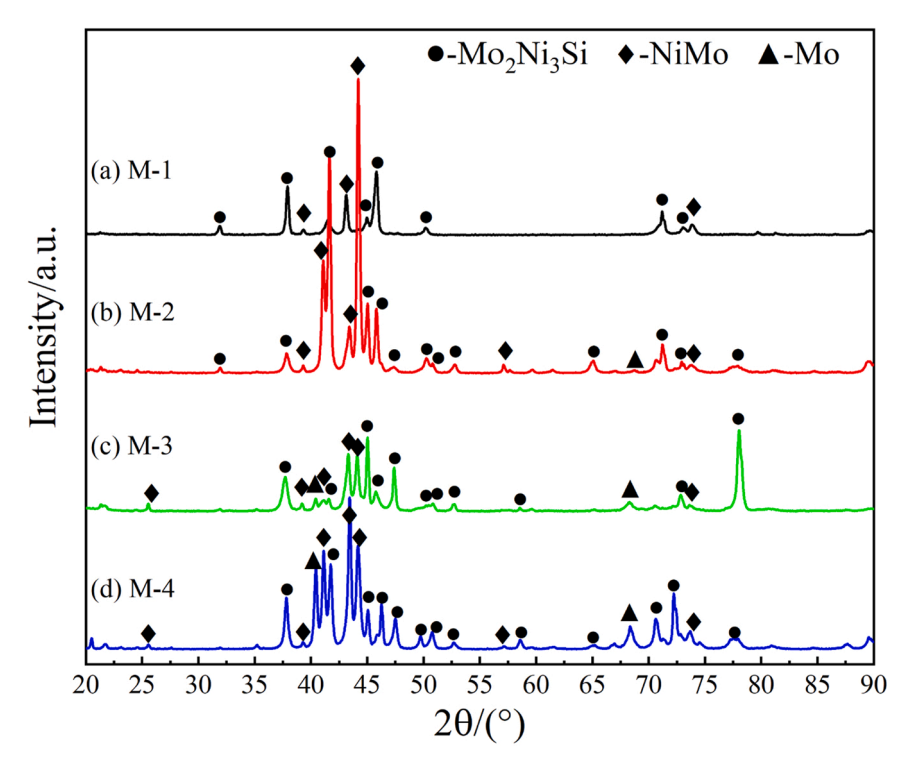


Fig. 2. XRD patterns of the Mo-Ni-Si alloys.

the main phases of the M-1 and M-2 samples were composed of the ternary metal silicide Mo_2Ni_3Si (JCPDS Card No. 15–0489) and the binary intermetallic compound NiMo (JCPDS Card No. 65–6903). Moreover, compared to the M-1 sample, the intensities of the diffraction peaks showed that the NiMo content in the M-2 sample was higher as the Mo content increased. With further increase in Mo content, in addition to the formation of Mo_2Ni_3Si and NiMo phases, elemental metal Mo was also present in M-3 and M-4 samples, which contributed to the fracture toughness of the alloys.

The typical microstructures of the Mo-Ni-Si alloys are shown in Fig. 3. The Mo-Ni-Si alloys have a uniform and dense structure, without noticeable porosity, inclusions, or defects. The microstructure of the alloys was gradually refined (in Fig. $3(a_1-d_1)$) and transitioned from a dual-phase structure (M-1 and M-2) to a three-phase structure (M-3 and M-4) as the Mo content increased. Fig. 4 shows the EDS elemental mapping of the Mo-Ni-Si alloys. Combining the XRD and EDS analysis results, it can be confirmed that for M-1 and M-2 samples, the primary dendritic phase (grey phase, orthorhombic crystal structure) and the

interdendritic phase (light grey phase, hp12-MgZn $_2$ Laves phase, C14 crystal structure) are intermetallic NiMo and Mo $_2$ Ni $_3$ Si, respectively. For the M-3 and M-4 samples, the primary dendritic phases were the refractory metal Mo, which was uniformly precipitated on the NiMo and Mo $_2$ Ni $_3$ Si substrates, as shown in Fig. 3(d) and Fig. 4(b). Moreover, the content of intermetallic NiMo and ductile metal Mo in the alloy increases with increasing Mo content. Among the three compositional phases, the refractory metal Mo has the highest melting point and was solidified firstly from the liquid phase, forming dendritic structures during the solidification process. Then, as the temperature further decreased and the elemental content of the liquid changed, the intermetallic NiMo was formed, and the remaining liquid was finally solidified in the form of metal silicide Mo $_2$ Ni $_3$ Si.

3.2. Mechanical properties of the Mo-Ni-Si alloys

The typical hardness indentation images, microhardness, fracture toughness and brittleness of the Mo-Ni-Si alloys were shown in Fig. 5. In

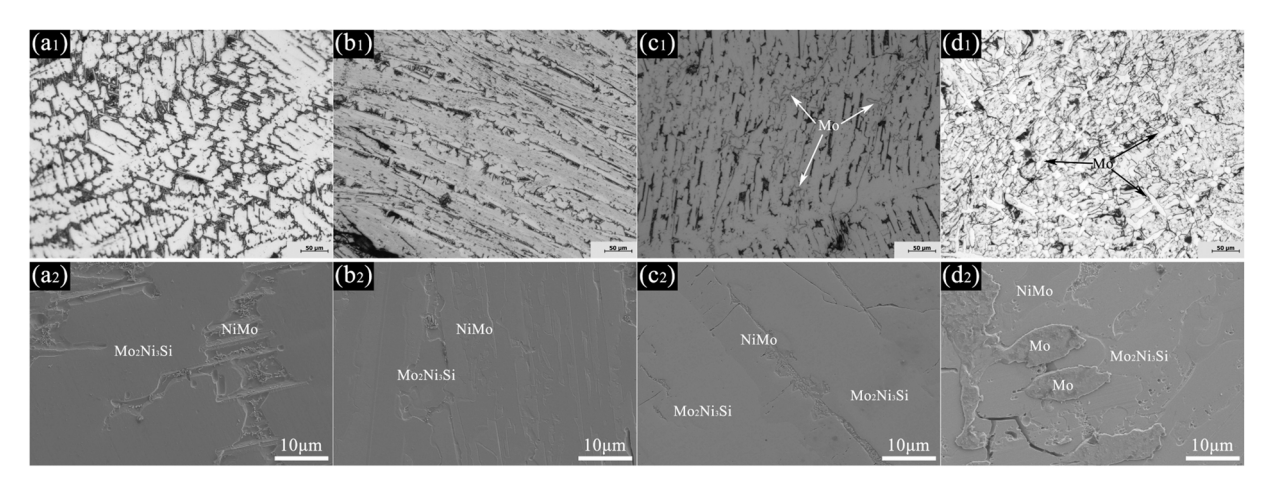


Fig. 3. OM images (a_1-d_1) and SEM micrographs (a_2-d_2) of the Mo-Ni-Si alloys. (a) M-1, (b) M-2, (c) M-3 and (d) M-4.

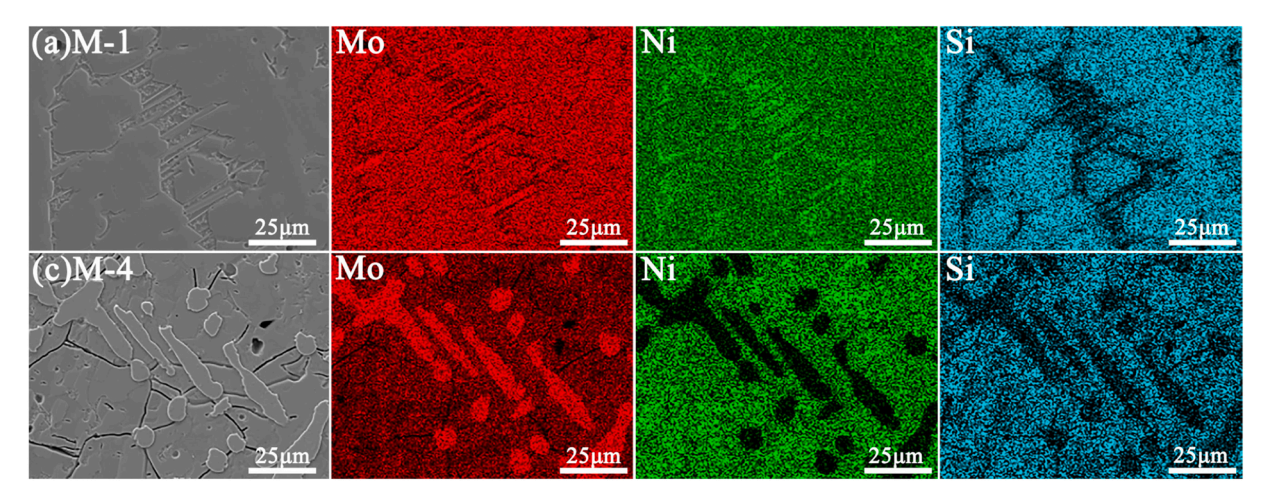


Fig. 4. EDS elemental mapping of the Mo-Ni-Si alloys. (a) M-1, and (b) M-4.

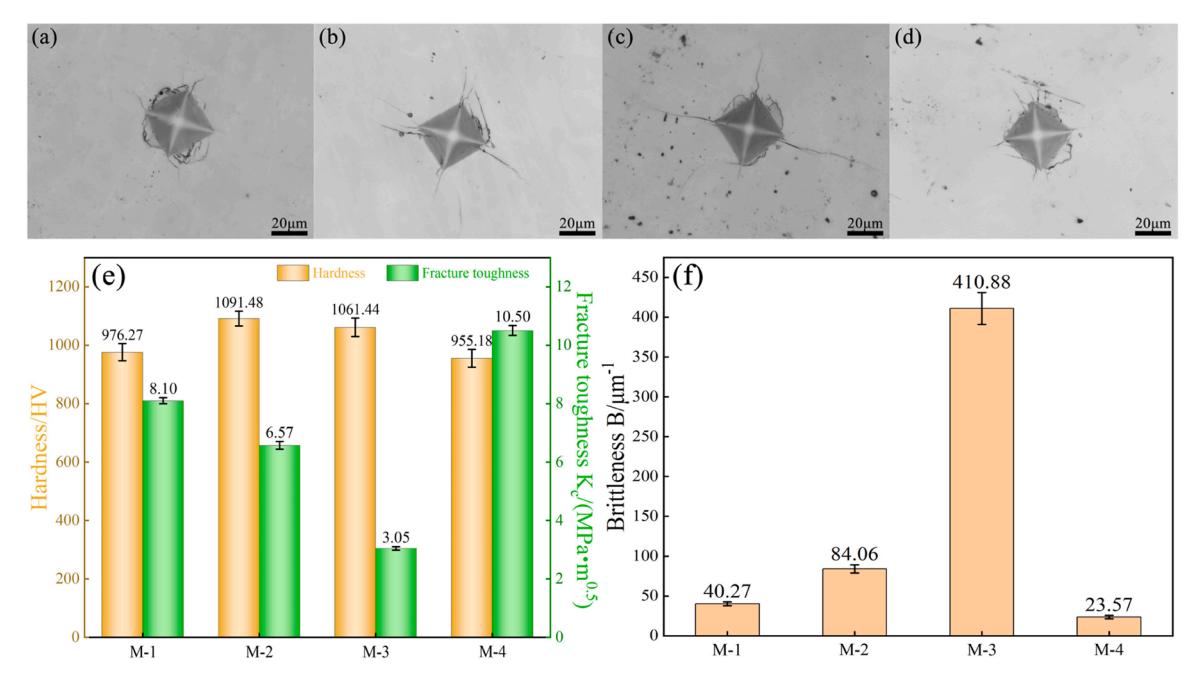


Fig. 5. Indentation image (a-d), hardness and fracture toughness (e), and the brittleness (f) of the Mo-Ni-Si alloys. (a) M-1, (b) M-2, (c) M-3 and (d) M-4.

Fig. 5(b, c), notable microcracks at the ends and edges of the diamondlike indentations of the M-2 and M-3 alloys were observed due to the intrinsic brittleness of the intermetallic NiMo and Mo₂Ni₃Si. Typically, long indentation microcracks indicate a low fracture toughness of the material. As observed in Fig. 5(e), the Mo-Ni-Si alloys exhibited high hardness ranging from 955 HV to 1091 HV. The fracture toughness of the Mo-Ni-Si alloys initially decreased and then increased with increasing Mo content. For the M-2 and M-3 samples, the alloys exhibited high hardness and low fracture toughness, which was consistent with the indentation crack lengths in Fig. 5(b, c). In contrast, the hardness indentation images of the M-4 sample exhibited a clear contour and had a higher fracture toughness (10.5 MPa·m^{1/2}) and relatively low hardness (955 HV) among all the samples (in Fig. 5(d and e)). This was attributed to the high content of the metal Mo in the M-4 alloy, which provides good plasticity and toughness. The brittleness B of the Mo-Ni-Si alloys was calculated according to the equation [28]:

$$B = \frac{H_v \cdot E}{K_c^2} \tag{2}$$

where H_{ν} is the material hardness, E is the modulus of elasticity, and K_c is the fracture toughness. The brittleness parameter compared the deformation process to the fracture process under applied load. The brittleness B of the materials increased with hardness and elastic modulus, and decreased with increasing fracture toughness. When the materials were more susceptible to surface fracture, the value of brittleness B was higher. In Fig. 5(f), the brittleness of the Mo-Ni-Si alloys initially increased and then decreased. The brittleness values of M-1, M-2, M-3, and M-4 alloys were 40, 84, 411, and 24 μ m⁻¹, respectively.

Fig. 6(a) shows the typical nano-indentation load-displacement curves for Mo-Ni-Si alloys. No significant protrusions were observed from the load-displacement curves, indicating that the loading only induced surface elastic-plastic deformations. For the selected indentation loads, the maximum displacements and the enclosed area surrounded by the loading-unloading curves of M-2 and M-3 alloys were smaller than those of M-1 and M-4 alloys. This suggests that the plastic deformation capacity of the M-2 and M-3 alloys was smaller, and their hardness and elastic modulus were higher, as shown in Fig. 6(b). The hardness and elastic modulus of the M-2 and M-3 alloys were (21.6 GPa and 339 GPa) and (19.4 GPa and 364 GPa), respectively. In general, the

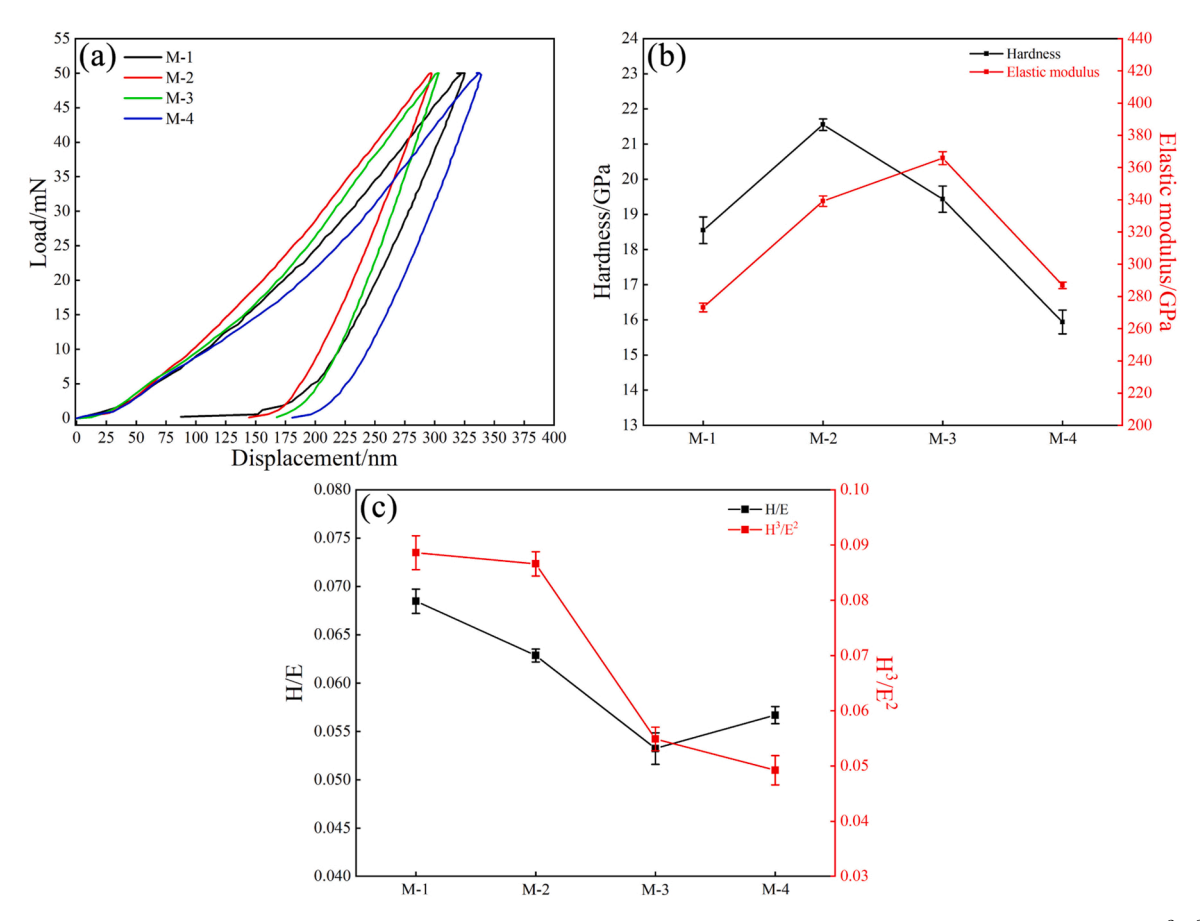


Fig. 6. Nanoindentation tests of the Mo-Ni-Si alloys. (a) load-displacement curves, (b) hardness and elastic modulus, and (c) H/E and H³/E².

H/E value was related to the fatigue damage resistance, and the $\mathrm{H}^3/\mathrm{E}^2$ value was likely to reflect the plastic deformation resistance during friction and wear [29]. The higher values of H/E and $\mathrm{H}^3/\mathrm{E}^2$ generally predicted that the mechanical performances and abrasion resistance of Mo-Ni-Si alloys were better. As depicted in Fig. 6(c), the Mo-Ni-Si alloys demonstrated a decreasing trend in their H/E and $\mathrm{H}^3/\mathrm{E}^2$ values with increasing Mo content. Among the alloys, the M-1 alloy exhibited the highest H/E and $\mathrm{H}^3/\mathrm{E}^2$ values, which predicts that the M-1 alloy possesses superior wear resistance compared to other alloys.

3.3. Tribocorrosion behaviors of the Mo-Ni-Si alloys

Fig. 7 shows the open circuit potential (OCP) and potentiodynamic polarization curves of Mo-Ni-Si alloys in 3.5 wt% NaCl solution. To ensure the electrochemical stability of the alloy surface, all samples were immersed in NaCl solution for 5 h before the electrochemical tests. In Fig. 7(a), the OCP values of Mo-Ni-Si alloys were relatively stable and more positive with increasing Mo content. In Fig. 7(b), the Mo-Ni-Si alloys showed a distinct passivation behavior, a wider passivation region and a lower passivation current density observed on the anodic polarization curves of the M4 alloy. The corrosion potential (E_{corr}), corrosion current density (i_{corr}) and breakdown potential (E_b) of the

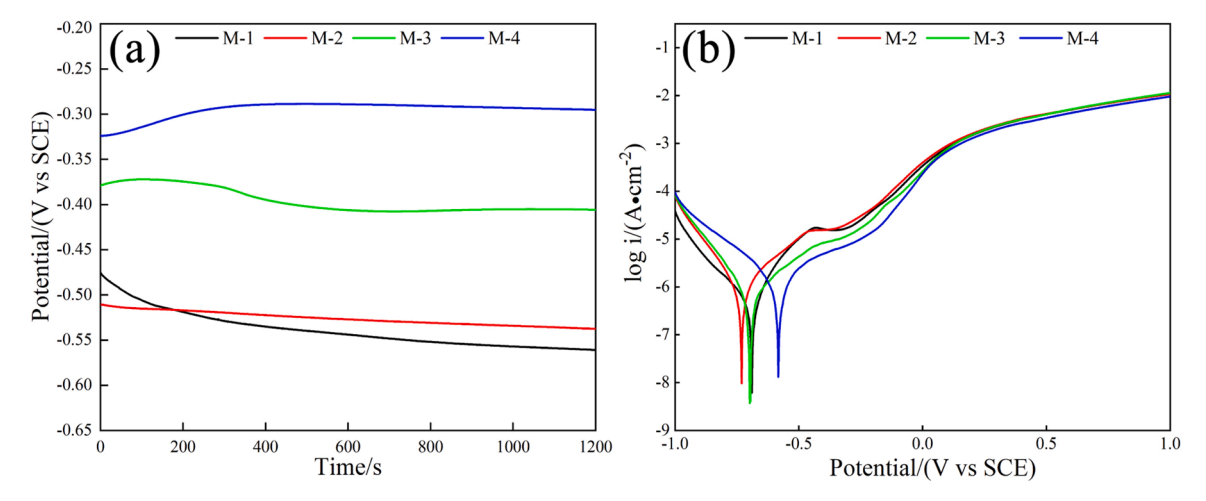


Fig. 7. Open circuit potential (a) and potentiodynamic polarization curves (b) of Mo-Ni-Si alloys in 3.5 wt% NaCl solution.

alloys are presented in Table 2. It can be observed that the alloys exhibit a more positive corrosion potential and breakdown potential, and a relatively stable corrosion current density with increasing Mo content. Therefore, high Mo content contributes to the electrochemical corrosion resistance of the Mo-Ni-Si alloys.

Fig. 8(a) illustrates the variation of OCP (vs. SCE) values and friction coefficients of Mo-Ni-Si alloys and 0Cr18Ni9 stainless steel sliding against Al₂O₃ balls under a 5 N load in 3.5 wt% NaCl solution before, during, and after the tribocorrosion tests. To ensure a stable electrochemical state, the 0Cr18Ni9 and Mo-Ni-Si alloys were soaked in NaCl solution for no less than 30 min before the onset of tribocorrosion. As illustrated in Fig. 8(a), the change in OCP values of all samples was negligible during immersion, indicating that the sample surfaces achieved a stable electrochemical state. Furthermore, with the increase of Mo content, The OCP value of M-4 samples was more positive than the other alloys, suggesting that metal Mo contributed to the corrosion resistance of Mo-Ni-Si alloys. Once tribocorrosion was initiated, a sharp decrease in the OCP value from -0.1 V to -0.28 V was observed for the 0Cr18Ni9 material, indicating that mechanical friction had damaged its surface passivation film. Compared to the surrounding passive region (as the cathode), the fresh metal at the wear track (as the anode) has higher electrochemical activity, and this difference in potential is prone to causing galvanic corrosion. In comparison, the OCP value of the Mo-Ni-Si alloy material decreases slightly and remains relatively stable compared to the OCr18Ni9. Notably, the OCP values of the M-1 and M-2 samples were almost unchanged before and after sliding contact. This demonstrated that the tribocorrosion properties and mechanisms of the Mo-Ni-Si alloys and the 0Cr18Ni9 material were different. In general, the tribocorrosion characteristics of a material depend on (1) the passivation characteristics of the material surface (the balance between passivation film breakdown and re-passivation, such as 0Cr18Ni9 stainless steel) (2) The mechanical properties, chemical stability and bonding characteristics of the material (such as Mo-Ni-Si alloys). Thus, Mo-Ni-Si alloys have good tribocorrosion resistance because of their high hardness and favorable chemical stability. Finally, with the end of sliding, the OCP values increased for all tested materials due to repassivation in NaCl solution on the material surface. In Fig. 8(a), the friction coefficients of Mo-Ni-Si alloys (M-1 to M-4) and 0Cr18Ni9 material sliding against Al₂O₃ balls were 0.112, 0.133, 0.111, 0.224 and 0.192, respectively. As the Mo content increases, the friction coefficients of the Mo-Ni-Si alloys initially decrease and then increase. The M-3 sample exhibited the lowest friction coefficient and stability. The changes in tribocorrosion curves of the M-3 sample under different loads are shown in Fig. 8(b). It can be seen that the OCP value of the M-3 sample decreased during tribocorrosion with increasing load. This was attributed to accelerated corrosion due to increased wear on the material surface and wider tribocorrosion tracks under higher loads. A decrease in OCP values with an increase in friction coefficient was observed in positions A and B of Fig. 8(b), indicating a strong wearaccelerated corrosion effect.

In order to analyze the synergistic process between wear and corrosion, tribocorrosion tests of M-2 and M-4 alloys were performed at a lower sliding frequency as shown in Fig. 9(a and b). The tribocorrosion curves and OCP of M-2 and M-4 alloys present almost similar features at all cyclic test sessions. That is, as the sliding started or stopped, the OCP values increased or decreased with an inverse relationship between the

 $\begin{tabular}{ll} \textbf{Table 2} \\ \textbf{The electrochemical parameters obtained from the polarization curves of Mo-Ni-Si alloys in 3.5 wt% NaC l solution.} \end{tabular}$

Samples	E_{corr} (V)	I_{corr} (μ A/cm ²)	E_b (V)
M-1	-0.690	0.5834	-0.3117
M-2	-0.731	0.9899	-0.3497
M-3	-0.698	0.432	-0.2814
M-4	-0.583	1.16	-0.2063

two, and this was in agreement with the results in Fig. 8. It can be seen that the tribocorrosion properties of the Mo-Ni-Si alloys in NaCl solution have good stability and reproducibility. From the partial enlargement in Fig. 9(c and d), it can be seen that there is a strong relationship between the coefficient of friction and the OCP within a sliding stroke (stages ①-④). In stage ①, with the coefficient of friction decreasing to zero, the OCP value increases because of the surface passivation of the alloys. In stage ②, the OCP value decreases with increasing friction coefficient due to the breakage of the surface passivation films. Afterward, the OCP values increase again as the friction coefficient decreases in stages ③ and ④.

The typical evolution of the friction coefficient and wear rates with varying loads in deionized water and 3.5 wt% NaCl solution were illustrated in Fig. 10. As shown in Fig. 10 (a-c), when sliding against Al₂O₃ balls in deionized water, the friction coefficients of 0Cr18Ni9 and Mo-Ni-Si alloys (M-1 to M-4) under 2 N, 5 N, and 10 N loads were (0.339, 0.083, 0.101, 0.075, 0.038), (0.322, 0.126, 0.109, 0.077, 0.025)and (0.304, 0.218, 0.1, 0.077, 0.038), respectively. Compared to the 0Cr18Ni9/Al₂O₃ pairs, the friction coefficients of the Mo-Ni-Si alloy/ Al₂O₃ pairs in deionized water were significantly lower, and no significant fluctuations under all loads. This demonstrated that the Mo-Ni-Si alloys exhibited excellent tribological performances in deionized water. Moreover, the friction coefficients of the alloys decreased with increasing Mo content as depicted in Fig. 10 (g). This was attributed to the formation of more MoOx, which enhances the lubrication environment on the wear track [30]. In contrast, in Fig. 10 (d-f), the friction coefficients of Mo-Ni-Si alloys were high and showed a significant fluctuation in 3.5 wt% NaCl solution. Moreover, as the Mo content increased, the friction coefficient of the alloys increased, whereas the friction coefficient decreased with increasing load (Fig. 10 (h)). This variation in the friction coefficient was inconsistent compared to that observed in the deionized solution, indicating that the friction mechanism of the alloys was different in the two solutions. In general, the friction coefficient was determined by a combination of the surface roughness and lubrication characteristics of the material. [31]. The material surface was subjected to the dual influences of corrosion and mechanical wear in the NaCl solution. The worn surfaces were more susceptible to corrosion because of the mechanical disruption of the passivation layer during sliding. Moreover, the surface corrosion of the Mo-Ni-Si alloys becomes more and more serious due to the mechanical-induced corrosion effect, which deteriorates the wear surface characteristics and causes the surface of the alloys to rougher by producing more wear debris and corrosion pits (in Fig. 11). Hence, the friction coefficient of the alloys was higher in NaCl solution compared to deionized water. As the Mo content increases, the amount of the easily corroded NiMo phase in the alloys increases. This leads to an uneven surface texture and increased friction coefficient due to the formation of galvanic corrosion. On the other hand, high applied loads facilitated the elimination of tribocorrosion products and corrosion defects, which also leads to a low friction coefficient of the alloy under high loads. Fig. 10 (i) shows the specific wear rates of 0Cr18Ni9 and Mo-Ni-Si alloys in deionized water and 3.5 wt% NaCl solution. The wear rates of the Mo-Ni-Si alloys were nearly 10 times lower compared to 0Cr18Ni9 material. Moreover, consistent with the trend of friction coefficient, the wear rate of Mo-Ni-Si alloys decreases with the increase of load. This indicated that Mo-Ni-Si alloys have a superior tribocorrosion performance in comparison to 0Cr18Ni9. For Mo-Ni-Si alloys, their surfaces were prone to forming a good protective film (MoO₃ - NiO - SiO₂) during the tribocorrosion process. MoO₃ has a good lubrication to lower the friction coefficient and wear rate, and the MoO3 - NiO - SiO2 passivation film has an excellent corrosion resistance [32], which contributed to the improvement of the tribocorrosion resistance of Mo-Ni-Si alloys.

Fig. 11 illustrates the SEM images and cross-sectional contours of tribocorrosion tracks for the 0Cr18Ni9 material and Mo-Ni-Si alloys in NaCl solution and deionized water at 5 N applied load. As depicted in

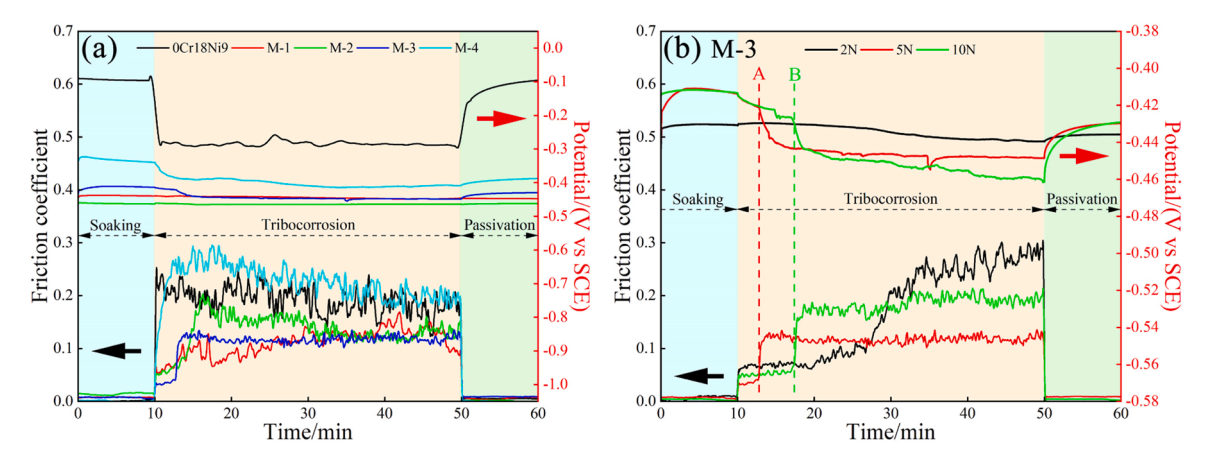


Fig. 8. OCP values and friction coefficients of Mo-Ni-Si alloys in 3.5 wt% NaCl solution. (a) Tribocorrosion testing of the alloys under a 5 N load, (b) Tribocorrosion testing of M-3 sample under various loads.

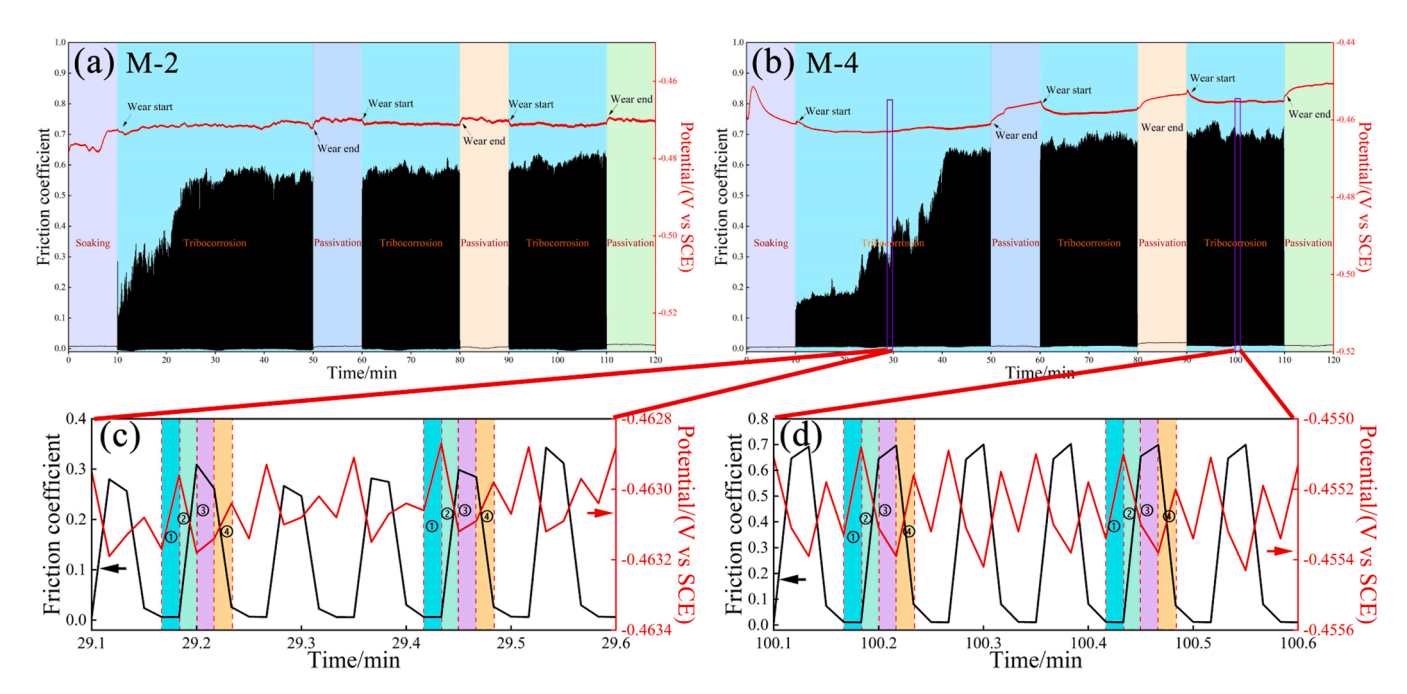


Fig. 9. (a and b) Tribocorrosion curves and the OCP values for M-2 and M-4 alloys during cyclic tribocorrosion test in 3.5 wt% NaCl solution at a sliding frequency of 0.2 Hz; (c and d) Local magnifications of the tribocorrosion curve and OCP value of the M-4 samples under different cycling tests.

Fig. 11 (a1-a3), the width and depth of wear tracks for OCr18Ni9 material in NaCl solution and deionized water are (493.6 μ m, 2.66 μ m) and (431.3 µm, 2.32 µm), respectively, which are significantly larger than those of Mo-Ni-Si alloys in both solutions. This indicates that Mo-Ni-Si alloys have better tribocorrosion resistance than 0Cr18Ni9 material in NaCl solution. In Fig. 11 (a1 and a2), apparent furrows, wear debris, or tribocorrosion products were observed within the wear track, implying that 0Cr18Ni9 stainless steel was severely worn. In Fig. 11 (a3-e3), the contours of the wear tracks for the 0Cr18Ni9 and Mo-Ni-Si alloys in 3.5 wt% NaCl solution were deeper and wider than those in deionized water, which was attributed to the corrosion-accelerated wear effect during the tribocorrosion tests. In Fig. 11 (b1 and b2), the wear track of the M-1 alloy was narrow and slight compared to the 0Cr18Ni9. However, some wear debris and tribocorrosion products were still observed on the wear tracks of the M-1 alloy. For the M-2 to M-4 alloys, the wear tracks became lighter and smoother compared to the M-1 alloy (Fig. 11 (c to e)), where the wear tracks were almost invisible. This showed that the tribocorrosion resistance of Mo-Ni-Si alloys was improved with the increase of Mo content. Moreover, as shown in the elemental mapping of Fig. 12, some O elements were distributed in the wear debris and NiMo inter-dendritic phase, suggesting that tribo-oxidation and selective tribocorrosion have occurred for the NiMo phase, which provided good lubrication characteristics during tribocorrosion tests of Mo-Ni-Si alloys in 3.5 wt% NaCl solution. From the above analysis, it was concluded that the primary tribocorrosion mechanism for the Mo-Ni-Si alloys was tribochemical wear.

To further explore the influence of applied load on the tribocorrosion characteristics of the Mo-Ni-Si alloys, the SEM images and cross-sectional contours of the wear tracks for the M-3 alloy under 2 N, 5 N, and 10 N loads were shown in Fig. 13. It can be observed that the M-3 alloy exhibited good tribocorrosion properties in 3.5 wt% NaCl solution and deionized water. Its surface wear was slight and some preliminary dendritic phases or scratches were visible under all loads, as shown in Fig. 13 (a1-c1 and a2-c2). Even so, a small number of shallow microgrooves and fine wear debris were consistently observed on the wear track of the M-3 alloy (see Fig. 13 b for the magnification of the localized area). The M-3 alloy has a high material brittleness (Fig. 5(f)), and when the Al $_2$ O $_3$ balls were sliding against the alloy, compressive and shear

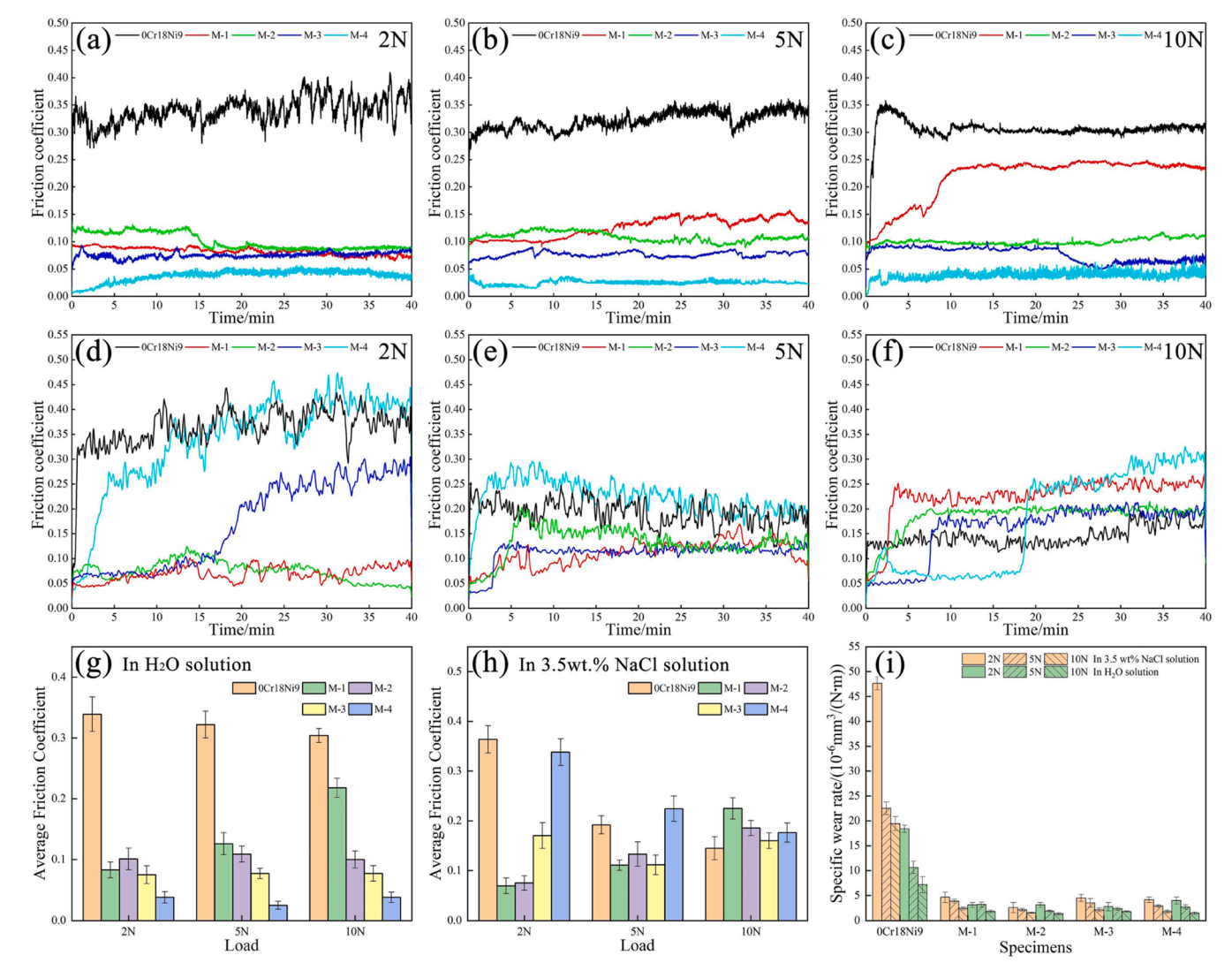


Fig. 10. Friction coefficients (a-f), average friction coefficient (g and h) and wear rates (i) of 0Cr18Ni9 stainless steel and Mo-Ni-Si alloys under different loads with lubrication by deionized water (a-c) and 3.5 wt% NaCl solution (d-f).

stresses were generated due to applied loads and sliding wear, resulting in surface spalling of the material. During the subsequent wear process, these flaked wear debris moved in the direction of sliding, scratching the worn surface. In Fig. 13 (a3-c3), the width and depth of the wear tracks for the alloy increased with the applied load. The wear debris and tribocorrosion products on the wear surfaces increased (Fig. 13 (c1-c2)) at 10 N load, indicating that the wear and corrosion increased at higher applied loads. Fig. 14 shows the TEM, HRTEM, and SAED images of wear debris of the M-3 alloy after the tribocorrosion test. The SAED pattern in Fig. 14 (b) showed six diffraction rings corresponding to the (110), (212), (220) planes of Mo₂Ni₃Si, (114), (226) planes of NiMo and (220) plane of Mo phase, respectively. In Fig. 14 (c), the calculated lattice spacings of the tribocorrosion particles were 0.2269 nm, 0.1801 nm, $0.1993 \; nm \; and \; 0.2079 \; nm, \; corresponding to the (110), (220), (112)$ planes of Mo_2Ni_3Si (PDF No. 15-0489) and the (114) plane of NiMo (PDF No. 65-6903), respectively.

3.4. Tribocorrosion mechanisms of Mo-Ni-Si alloys

The combined effect of material losses induced by wear and corrosion during tribocorrosion tests was investigated by Watson et al. [33]. The total tribocorrosion volume loss (V_T) was calculated using the equation:

$$V_T = V_C + V_W + \Delta V \tag{1}$$

$$\Delta V = V_{WC} + V_{CW} \tag{2}$$

where, V_C is pure corrosion, V_W is pure wear, ΔV is the material loss under the combined action of wear and corrosion, V_{WC} is corrosion caused by wear, and V_{CW} is wear caused by corrosion. The V_T and V_W of 0Cr18Ni9 and Mo-Ni-Si alloys were the wear volume loss in 3.5 wt% NaCl solution and deionized water, respectively. It could be calculated according to the formula: V = LA, L is the length of the wear scar (5 mm), A is the contour area of the wear scar obtained from Fig. 11 (a3e3), and the calculated results are presented in Table 3. V_C and V_{WC} could be calculated by detecting the content of metal ions in the tribocorrosion solutions using the high-resolution inductively coupled plasma optical emission spectrometer (ICP-OES) method [34]. T. Mathew et al. [35] measured the tribocorrosion loss of CoCrMo alloy in NaCl solution using the wear mark profile method and the metal ion content method (ICP-MS), respectively. The results showed good agreement between the two approaches. However, a small amount of metal ions may precipitate that cannot be detected by the ICP-OES method, which results in slightly lower measured values of tribocorrosion loss. In addition, corrosion did not completely dissolve the alloy but instead formed a loose structure that accelerated wear, which also

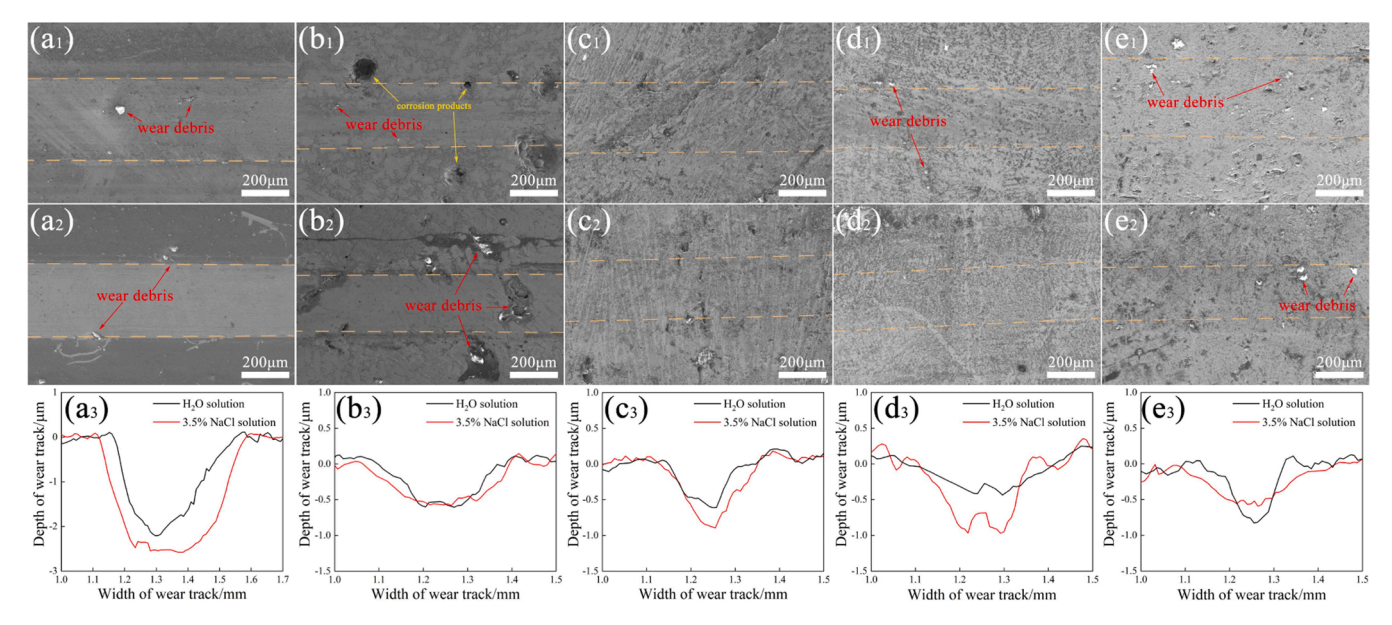


Fig. 11. SEM images and wear contours (a_3-e_3) of wear tracks on the 0Cr18Ni9 and Mo-Ni-Si alloys in 3.5 wt% NaCl solution (a_1-e_1) and deionized water (a_2-e_2) under 5 N applied load.

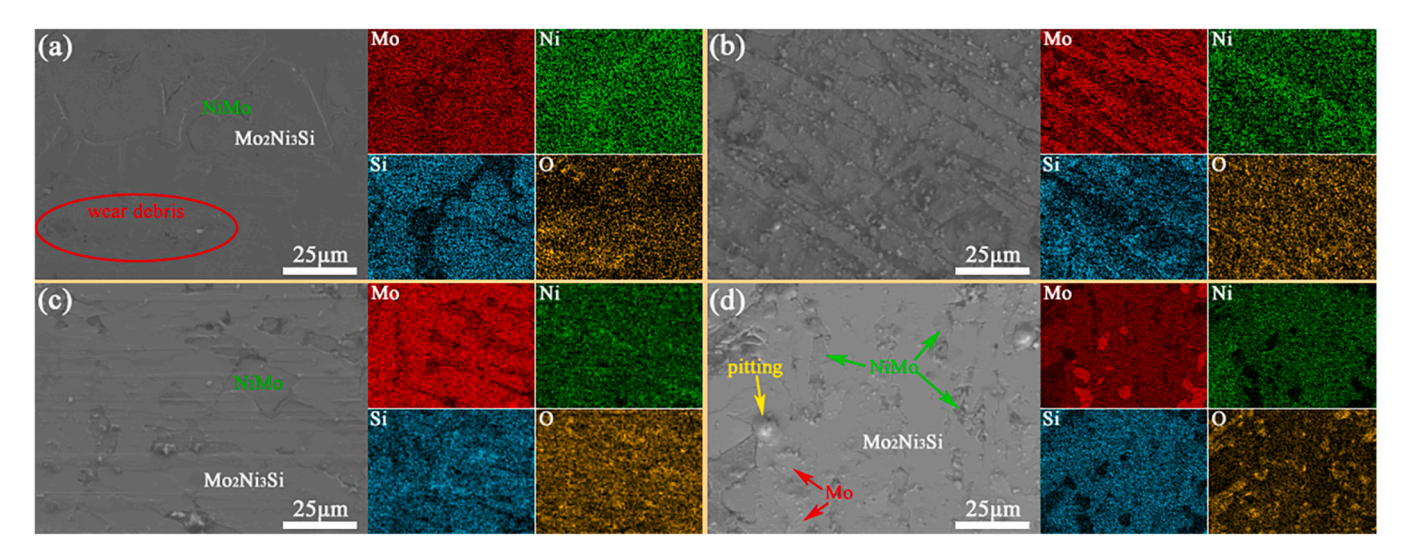


Fig. 12. SEM images and corresponding EDS elemental mapping of wear tracks for the Mo-Ni-Si alloys in 3.5 wt% NaCl solution (a) M-1, (b) M-2, (c) M-3, and (d) M-4 alloy.

contributed to the deviation in tribocorrosion loss measurement. Fig. 15 shows the ICP-OES analysis results of the tribocorrosion solutions for Mo-Ni-Si alloys. It was observed that the contents of metal ions in the tribocorrosion solutions decreased from M-1 to M-3 alloys, indicating that the improvement in corrosion and tribocorrosion resistance of the alloys increased with the Mo contents. However, the elevated metal ions in the tribocorrosion solution of the M-4 alloys compared to the M-3 alloys, especially the proportion of Ni and Mo ions was significantly higher (in Fig. 15 (b)), indicating that the selective tribocorrosion occurred for the NiMo phase. This was consistent with the results of the SEM images and EDS analysis in Fig. 12 (d). According to Fig. 14, V_C and V_{WC} ($V=m/\rho$, m is the ions mass in solution and ρ is the material density) were calculated and the results are shown in Table 3.

To further analyze the tribocorrosion mechanism, Fig. 16 shows the contribution of tribocorrosion components and $\Delta W/\Delta C$ values for 0Cr18Ni9 and Mo-Ni-Si alloys. In Fig. 16 (a), the material loss of 0Cr18Ni9 material was mainly composed of three aspects: V_W (46.3%), V_{CW} (38.33%) and V_C+V_{WC} (15.37%). For easily passivated materials

(0Cr18Ni9 and Mo-Ni-Si alloys), the materials volume loss caused by pure corrosion (V_C) was negligible [4,36]. Thus, the proportion of wear loss caused by the synergistic effect ($V_{CW} + V_{WC}$) was 53.7%, which suggested that the synergistic effect of wear and corrosion plays a major role in the tribocorrosion process of 0Cr18Ni9 in 3.5 wt% NaCl solutions. For all Mo-Ni-Si alloys, it was evident that pure wear was the major cause of material loss. In contrast, the influence of tribocorrosion losses induced by corrosion factors (V_C+V_{WC}) on Mo-Ni-Si alloys was weak. The percentage of (V_C+V_{WC}) for all alloys is less than 3.93%. Moreover, the percentage of material loss due to the combined effect of wear and corrosion ($V_{CW}+V_{WC}$) decreased from 17.79% for M-1 alloys to 7.14% for M-4 alloys, suggesting that a high Mo content improves the corrosion and tribocorrosion resistance of the alloys. Meanwhile, high hardness, good chemical stability and surface passivation layers (MoO₃, NiO and SiO₂) also contribute to improving the tribocorrosion performance of Mo-Ni-Si alloys in NaCl solution. It is noteworthy that the percentage of ($V_{CW}+V_{WC}$) for M-3 alloys was significantly higher than that of other Mo-Ni-Si alloys. This is probably caused by the fact that the

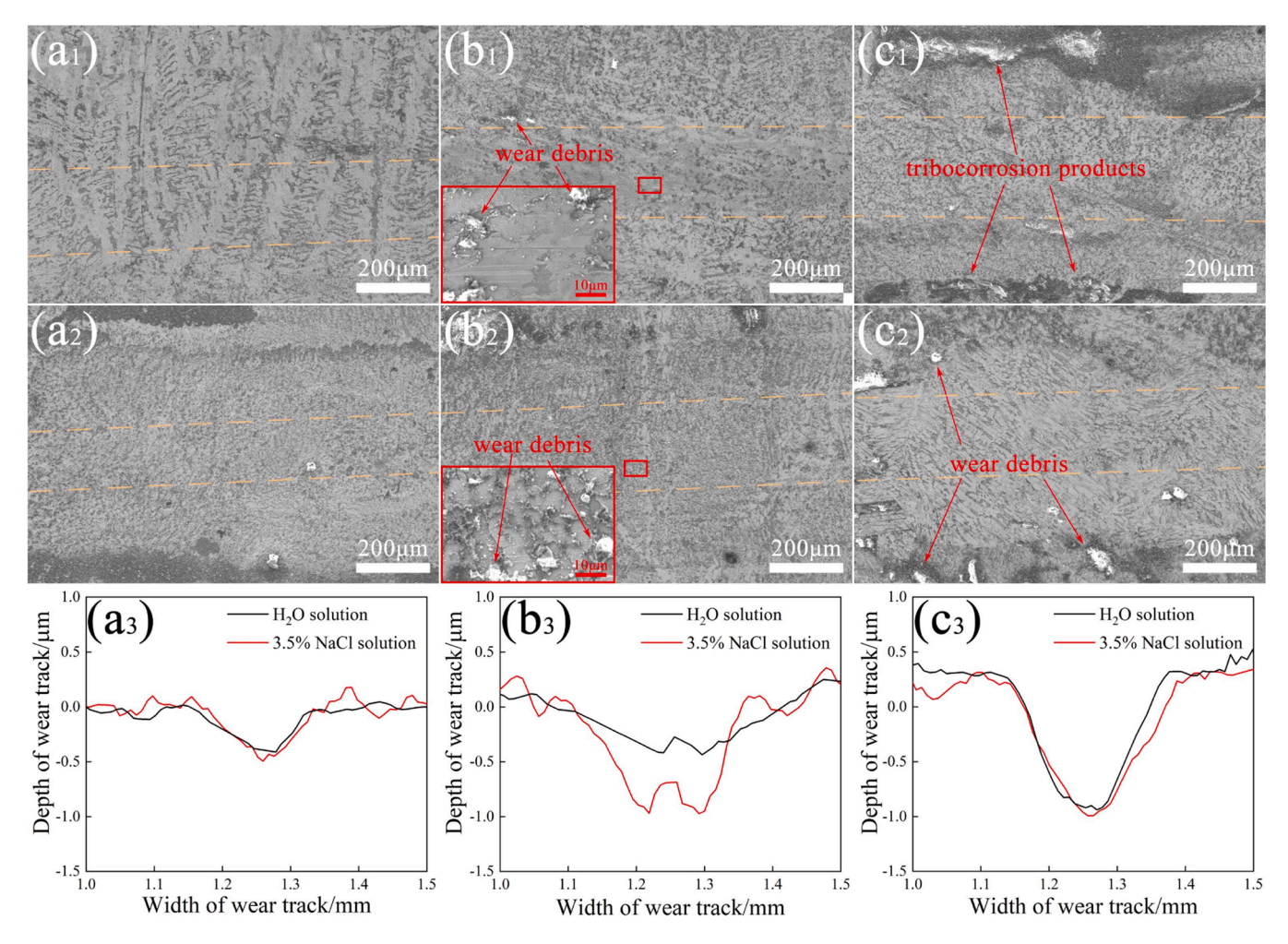


Fig. 13. SEM images and wear contours (a_3-c_3) of wear tracks on M-3 alloy in 3.5 wt% NaCl solution (a_1-c_1) and deionized water (a_2-c_2) under 2 N (a_1-a_3) , 5 N (b_1-b_3) and 10 N (c_1-c_3) applied load.

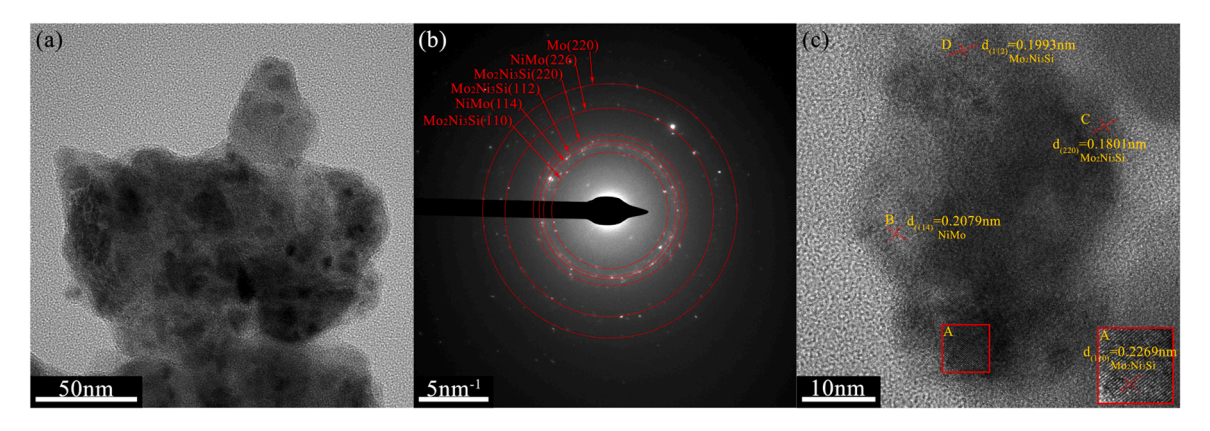


Fig. 14. High-resolution transmission electron microscopy (HRTEM) observations of wear debris for the M-3 alloy after tribocorrosion test.

 $\begin{tabular}{ll} \textbf{Table 3} \\ \textbf{Wear volume loss of 0Cr18Ni9 and Mo-Ni-Si alloys after tribocorrosion tests} \\ \textbf{under 5 N loads}. \\ \end{tabular}$

Samples	$V_T (\mathrm{mm}^3)$	$V_W (\mathrm{mm}^3)$	$V_{CW} (\mathrm{mm}^3)$	$V_C+V_{WC} (\mathrm{mm}^3)$
0Cr18Ni9	5.4 E - 3	2.5 E - 3	2.07 E - 3	8.27 E - 4
M-1	9.33 E - 4	7.67 E - 4	1.33 E - 4	3.34 E - 5
M-2	5.16 E - 4	4.5 E - 4	4.57 E - 5	2.03 E - 5
M-3	8.5 E - 4	5.67 E - 4	2.72 E - 4	1.04 E - 5
M-4	7.0 E - 4	6.5 E - 4	3.75 E - 5	1.25 E - 5

M-3 alloy surface has more thermal stress microcracks because of its high material brittleness (see Fig. 5(f)), which accelerates the tribocorrosion. Stack et al. [37,38] proposed a wear-corrosion region mapping to analyze the tribocorrosion mechanism, as follows:

$$S = \Delta W / \Delta C \tag{3}$$

$$\Delta W = (V_W + V_{CW})/V_T \tag{4}$$

$$\Delta C = (V_C + V_{WC})/V_T \tag{5}$$

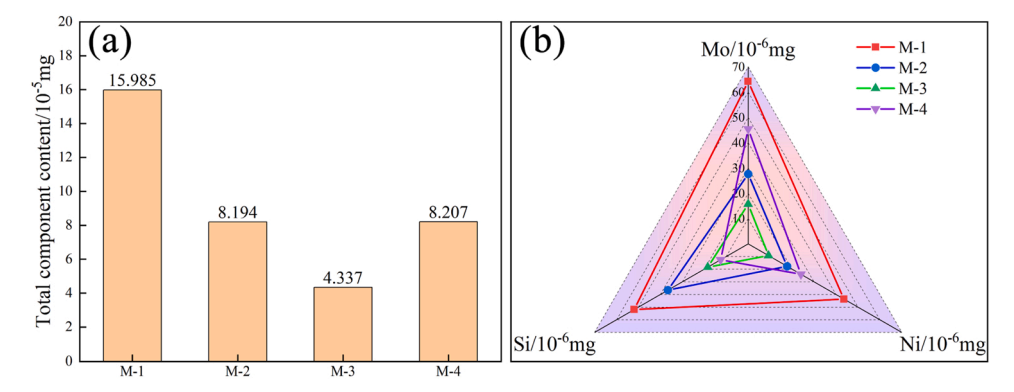


Fig. 15. ICP-OES analysis results of the tribocorrosion solutions for Mo-Ni-Si alloys. (a) Total component content, (b) Content of elemental components.

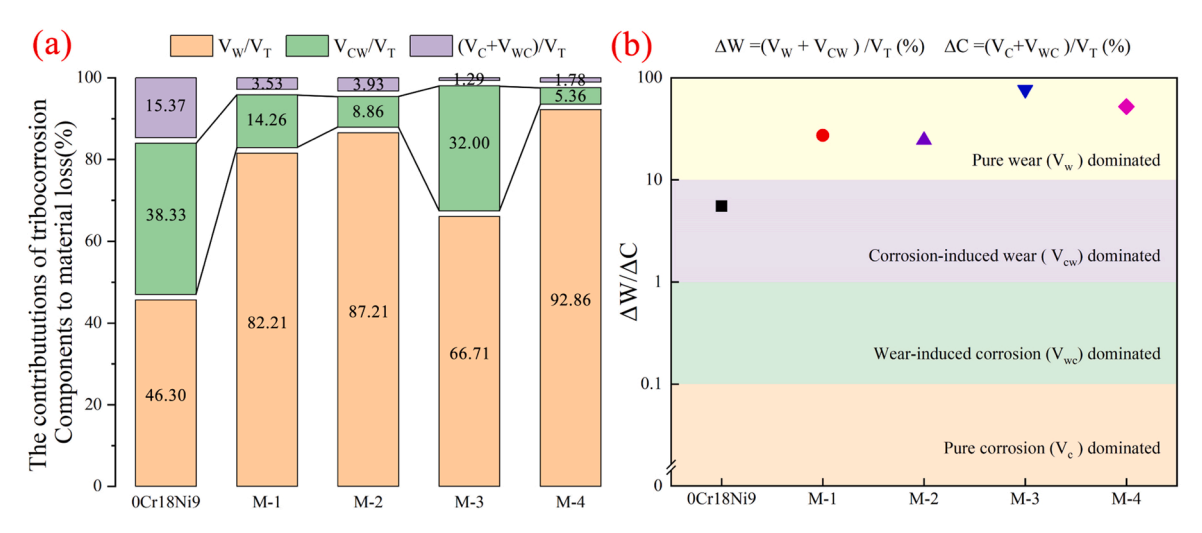


Fig. 16. Contributions of tribocorrosion components (a) and $\Delta W/\Delta C$ values (b) for 0Cr18Ni9 and Mo-Ni-Si alloys sliding against Al₂O₃ balls in 3.5 wt% NaCl solution.

It is generally considered that when 0 < S < 0.1, 0.1 < S < 1, 1 < S< 10, and S > 10, the corresponding tribocorrosion mechanisms are pure corrosion (V_C) , wear-induced corrosion (V_{WC}) , corrosion-induced wear (V_{CW}) , and pure wear (V_W) dominated, respectively. As shown in Fig. 16 (b), the $\Delta W/\Delta C$ point for the 0Cr18Ni9 material appeared in the corrosion-induced wear (V_{CW}) dominated region, indicating that the corrosion-induced wear loss had a significant impact during the tribocorrosion test. However, all the points for the Mo-Ni-Si alloys appeared in the region dominated by pure wear, which predicted that the wear behaviors were the main mechanism of tribocorrosion loss for the alloys in NaCl solution under OCP conditions. This was because the alloy phase composition (Mo2Ni3Si, NiMo intermetallic compound) has better electrochemical stability than 0Cr18Ni9 stainless steel. In addition, the alloys have a high Mo content, and the formation of a MoO₃ passivation layer on the wear track contributes to achieving good lubrication characteristics and improving tribocorrosion resistance [3,39].

4. Conclusions

Mo-Ni-Si alloys were fabricated by the arc melting method. The structure and tribocorrosion characteristics of the alloys in 3.5 wt% NaCl solution were investigated. The results were summarized as follows:

(1) The alloys have high hardness (~1000 HV), elastic modulus, and a good strength and toughness combination, and are mainly composed of high-strength Mo₂Ni₃Si, NiMo intermetallic and Mo_{ss} toughness phases. With increasing Mo content, the fracture

- toughness of the Mo-Ni-Si alloys initially decreased and then increased, while the material brittleness showed the opposite trend.
- (2) Mo-Ni-Si alloys exhibited more favorable tribocorrosion characteristics compared to 0Cr18Ni9 material in 3.5 wt% NaCl solution because of their high hardness, good chemical stability and the well-lubricated MoO₃-NiO-SiO₂ protective layer formed on the surface. Meanwhile, the OCP values of the alloys are inversely related to the friction coefficient during the tribocorrosion tests, which is attributed to the synergistic effect of wear and corrosion.
- (3) The wear rates of Mo-Ni-Si alloys were approximately one order of magnitude lower compared to 0Cr18Ni9 stainless steel. The friction coefficient and wear rates of Mo-Ni-Si alloys decrease with increasing load. For 0Cr18Ni9 stainless steel, the main tribocorrosion mechanism was dominated by corrosion-induced wear. However, the tribocorrosion losses of Mo-Ni-Si alloys were mainly attributed to the pure wear behavior and selective tribocorrosion of the interdendritic phase (NiMo).

CRediT authorship contribution statement

Hui chen: Writing – review & editing, Investigation, Funding acquisition, Formal analysis. **Z. Zhang:** Writing – original draft, Investigation. **X.L. Zhao:** Writing – original draft, Data curation. **R.P. Li:** Writing – review & editing, Writing – original draft, Investigation, Formal analysis. **L.Y. Liu:** Investigation, Data curation.

Declaration of Competing Interest

The authors declare that they have no known competing financial interests or personal relationships that could have appeared to influence the work reported in this paper.

Data availability

Data will be made available on request.

Acknowledgments

This research was supported by the Natural Science Foundation of Shandong Province of China (Grant Nos. ZR2021ME204), and the National Natural Science Foundation of China (Grant Nos. 52301207). The authors acknowledge Mr Deshun Liu for their assistance in the experiments of the nanoindentation test.

References

- Zhang XS, Chen YJ, Hu JL. Recent advances in the development of aerospace materials. Prog Aerosp Sci 2018;97:22–34.
- [2] Nie RF, Huang YJ, Li XW, Li DY, Ying JW. Bond of epoxy—coated reinforcement to seawater coral aggregate concrete. Ocean Eng 2020;208:107350.
- [3] Fu YQ, Zhou F, Zhang MD, Wang QZ, Zhou ZF. Structure and tribocorrosion behavior of CrMoSiCN nanocomposite coating with low C content in artificial seawater. Friction 2021;9:1599–615.
- [4] Chen H, Zhang Z, Hao XH, Huang BX, Zhao XC, Hu CC. Microstructure and tribocorrosion properties of NiTi/AlNi₂Ti ternary intermetallic alloy. Vacuum 2021:184:109928.
- [5] Li ZY, Yu HY, Sun DB. The tribocorrosion mechanism of aluminum alloy 7075-T6 in the deep ocean. Corros Sci 2021;183:109306.
- [6] Panagopoulos CN, Georgiou EP, Markopoulos C. Corrosion and wear of zinc in various aqueous based environments. Corros Sci 2013:70:62–7.
- [7] Zhou R, Sun GF. Laser alloying with Mn+Cr₃C₂ and Mn+NiCr-C for improved wear and corrosion resistance of stainless steel. Surf Coat Technol 2022;451:129076.
- [8] Gong LQ, Fu HG, Zhi XH. Corrosion wear of hypereutectic high chromium cast iron: a review. Metals 2023;13:308.
- [9] Hu HR, Guo YJ, Yan JH, Qiu JW, Wang Y. Dry sliding wear behavior of MoSi₂-Mo₅Si₃-Mo₅SiB₂ composite at different temperatures and loads. Wear 428 2019: 237–45
- [10] Xu J, Liu L, Li Z, Munroe P, Xie ZH. Niobium addition enhancing the corrosion resistance of nanocrystalline Ti₅Si₃ coating in H₂SO₄ solution. Acta Mater 2014;63:
- [11] Yin YX, Wang HM. High-temperature wear behaviors of a laser melted Cu_{ss}/ (Cr₅Si₃-CrSi) metal silicide alloy. Mat Sci Eng A 2007;452-453;746–50.
- [12] Zhang JX, Chen BM, Yue W, Chen H. Phase composition, microstructure, and wear properties of Ni/Ni₃Si composites prepared by mechanical alloying. J Superhard Mater 2021;43:12–20.
- [13] Matsunoshita H, Sasai Y, Fujiwara K, Kishida K, Inui H. Plastic deformation of directionally solidified ingots of binary and some ternary MoSi₂/Mo₅Si₃ eutectic composites. Sci Technol Adv Mater 2016;17:517–29.
- [14] Xu J, Zhou CH, Chen ZF, Wang Y, Jiang SY. Corrosion behaviors of (Cr, Fe)₃Si/Cr₁₃Fe₅Si₂ composite coating under condition of synergistic effects of electrochemical corrosion and mechanical erosion. J Alloy Compd 2010;496: 429–32.

- [15] Liu J, Zhang J, Deng LJ, Hao GN. Microstructure and corrosion behaviour of laser-cladded γ-Ni/Mo₂Ni₃Si alloy coating. Surf Eng 2019;35:59–65.
- [16] Huang BY, Song CY, Liu Y, Gui YL. Microstructure characterization and wearresistant properties evaluation of an intermetallic composite in Ni-Mo-Si system. Materials 2017;10:130.
- [17] Gui YL, Qi XJ, Song CY. Metallic tribological compatibility of Mo_{SS}-toughened Mo₂Ni₃Si metal silicide alloys. Mater Sci Forum 2012;704:1068–72.
- [18] Tan H, Sun QC, Chen JJ, Zhu SY, Cheng J, Yang J. Dry sliding tribological properties and wear mechanisms of Mo-Si-B-xTi alloys at the temperature range of 25-1000 °C. Tribol Int 2023;177:107897.
- [19] Xu YW, Wang HM. Microstructure and wear properties of laser melted γ -Ni/Mo₂Ni₃Si metal silicide "in situ" composite. Mater Lett 2007;61:412–6.
- [20] Gui YL, Wang HM. Microstructure and dry sliding wear resistance of Mosstoughened Mo₂Ni₃Si metal silicide alloys. Int J Refract Met H 2007;25:433–9.
- [21] Song CY, Gui YL, Kuang SB, Wang SH, Zhao DG. Microstructure and wear resistance of a novel Mo-Ni-Si system intermetallic composite with ductile Mo phase. Mater Trans 2016;57:721–5.
- [22] Lu XD, Wang HM. High-temperature sliding wear behaviors of laser clad Mo₂Ni₃Si/ NiSi metal silicide composite coatings. Appl Surf Sci 2003;214:190–5.
- [23] Gui YL, Song CY, Wang SH, Zhao DG. Elevated-temperature wear behaviors of NiMo/Mo₂Ni₃Si intermetallic "in situ" composites. J Mater Res 2016;31:66–75.
- [24] Xu YW, Wang HM. Microstructure and room temperature dry sliding wear behavior of Mo₂Ni₃Si/γ dual phase alloy. Acta Metall Sin 2006;42:722–6.
- [25] Liu J, Zhang J, Liu PC, Deng LJ, Zhang S. Microstructure and wear behaviour of laser-cladded γ-Ni_{ss}/Mo₂Ni₃Si coating, Surf Eng 2020;36:1270–7.
- [26] Xu YW, Wang HM. Room-temperature dry sliding wear behavior of γ-Ni/Mo₂Ni₃Si metal silicide "in situ" composites. J Alloy Compd 2007;440:101–7.
- [27] Kulka M, Makuch N, Piasecki A. Nanomechanical characterization and fracture toughness of FeB and Fe₂B iron borides produced by gas boriding of Armco iron. Surf Coat Technol 2017;325:515–32.
- [28] Quin JB, Quin GD. Indentation brittleness of ceramics: a fresh approach. J Mater Sci 1997;32:4331–46.
- [29] Fu YQ, Zhou F, Zhang MD, Wang QZ, Zhou ZF. Structural, mechanical and tribocorrosion performances of CrMoSiN coatings with various Mo contents in artificial seawater. Appl Surf Sci 2020;525:146629.
- [30] Fu YQ, Zhou F, Wang QZ, Zhang MD, Zhou ZF. Electrochemical and tribocorrosion performances of CrMoSiCN coating on Ti-6Al-4V titanium alloy in artificial seawater, Corr. Sci 2020;165:108385.
- [31] Ma FL, Li JL, Zeng ZX, Gao YM. Structural, mechanical and tribocorrosion behavior in artificial seawater of CrN/AlN nano-multilayer coatings on F690 steel substrates. Appl Surf Sci. 2018:428:404–14.
- [32] Zhang MD, Zhou F, Wang QZ, Fu YQ, Zhou ZF. Structural and tribological properties of CrMoCN coatings with various Mo contents in artificial seawater. Appl Surf Sci 2019;493:485–96.
- [33] Watson SW, Friedersdorf FJ, Madsen BW, Cramer SD. Methods of measuring wear corrosion synergism. Wear 181 1995:476–84.
- [34] Li RP, Chen H, Hao XH, Zhao XC, Huang BX. Microstructure, mechanical properties and tribocorrosion characteristics of (Mo_{1-x}Cr_x)₅Si₃ alloys. Int J Refract Met H 2023:115:106291.
- [35] Mathew MT, Uth T, Hallab NJ, Pourzal R, Fischer A, Wimmer MA. Construction of a tribocorrosion test apparatus for the hip joint: validation, test methodology and analysis. Wear 2011;271:2651–9.
- [36] Shan L, Wang YX, Zhang YR, Zhang Q, Xue QJ. Tribocorrosion behaviors of PVD CrN coated stainless steel in seawater. wear 2016;362-363:97–104.
- [37] Stack MM, Pungwiwat N. Erosion–corrosion mapping of Fe in aqueous slurries: some views on a new rationale for defining the erosion–corrosion interaction. Wear 2004;256:565–76.
- [38] Stack MM, Abd El Badia TM. Mapping erosion-corrosion of WC/Co-Cr based composite Particle velocity and applied potential effects. Surf Coat Technol 2006; 201:1335-47
- [39] Lee HB, Wu MY. A study on the corrosion and wear behavior of electrodeposited Ni–W–P coating. Metall Mater Trans A 2017;48:4667–80.